

Numerical study of airfoil thickness effects on the performance of J-shaped straight blade vertical axis wind turbine

Mahdi Zamani¹, Mohammad Javad Maghrebi^{*1} and Sajad A. Moshizi²

¹Department of Mechanical Engineering, Ferdowsi University of Mashhad, Mashhad, Iran

²Sun-Air Research Institute, Ferdowsi University of Mashhad, Mashhad, Iran

(Received August 16, 2015, Revised March 16, 2016, Accepted March 24, 2016)

Abstract. Providing high starting torque and efficiency simultaneously is a significant challenge for vertical axis wind turbines (VAWTs). In this paper, a new approach is studied in order to modify VAWTs performance and cogging torque. In this approach, J-shaped profiles are exploited in the structure of blades by means of eliminating the pressure side of airfoil from the maximum thickness toward the trailing edge. This new profile is a new type of VAWT airfoil using the lift and drag forces, thereby yielding a better performance at low TSRs. To simulate the fluid flow of the VAWT along with J-shaped profiles originated from NACA0018 and NACA0030, a two-dimensional computational analysis is conducted. The Reynolds Averaged Navier-Stokes (RANS) equations are closed using the two-equation Shear Stress Transport (SST) turbulence model. The main objective of the study is to investigate the effects of J-shaped straight blade thickness on the performance characteristics of VAWT. The results obtained indicate that opting for the higher thickness in J-shaped profiles for the blade sections leads the performance and cogging torque of VAWT to enhance dramatically.

Keywords: VAWT; J-shaped Profile; thickness; numerical simulation; cogging torque

1. Introduction

Nowadays, there is abundant need to eliminate non-renewable energy arising from fossil fuels due to finite supply and environmental impacts. Many researches have been documented about renewable energy technologies such as Ghasemi *et al.* (2015) and Khare *et al.* (2016). Wind energy as a renewable energy has been received significant attention for power production during the last decade, on the grounds that wind turbines produce electrical power as a carbon free power generation. Wind turbines are classified according to the orientation of the axis of the rotor to the ground into two general types: horizontal axis wind turbine (HAWT) and vertical axis wind turbine (VAWT). VATWs have several outstanding advantages in comparison to HAWTs such as omni-directionality, simplicity of manufacturing and mechanically withstanding higher wind speeds, leading to attract considerable attention. As can be predicted, there is a series of underlying complex structures in the fluid flow of VATWs due to existing wake along with complex flow structures including different length scales, high directional variability, large skew angles and

*Corresponding author, Ph.D., E-mail: mjmaghrebi@um.ac.ir

increased turbulence intensity (Siddiqui *et al.* 2015).

According to the aerodynamic principles, small VAWTs are categorized into drag-based and lift-based. Among the drag-based VAWT, the first and simplest type of these mechanisms was designed by Savonius (1931). The Savonius turbine consists of a rotor with two cups (half cylinders) in different directions exposed to the wind, one with the concave surface and the other with convex surface. The concave surface leads to rotate the rotor, because the drag coefficient induced in the concave surface is more than that in convex surface. The Savonius rotor has many advantages over the other conventional wind turbines, such as simple and cheap construction, acceptance of wind from any direction, relatively low operation speed (rpm) and high starting torque (Modi and Fernando 1989). Despite all of the aforementioned advantages, a disadvantage of Savonius turbine which may outweigh its advantages is its low efficiency. The maximum averaged power coefficient reported by many researchers (Kamoji *et al.* 2009, Fujisawa 1992, Fernando and Modi 1989, Saha *et al.* 2008, Menet 2004) includes values around 0.05-0.3, for many turbine settings (Akwa *et al.* 2012).

Another wind rotor is the lift-based VAWT originally designed by Darrieus (1931). The Darrieus wind rotor consists of airfoil-shaped blades of constant chord length attached to a rotating vertical shaft. Although the Darrieus turbines have high efficiency, they have a low cogging torque. The Darrieus turbines have a limited self-starting capacity unlike the Savonius type because there is often insufficient torque to overcome friction at startup. This is largely because lift forces on the blades are small at low rotational speeds and for two-bladed machines in particular the torque generated is virtually the same for each of the stationary blades at startup, irrespective of the rotor azimuth angle relative to the incident wind direction (Tong 2010). In addition, the blade airfoils of a Darrieus rotor are set on their stall regions at low tip speed ratios for most azimuth angles. Consequently, the Darrieus turbines generally need to be run up to a sufficiently high tip speed for the rotor to accelerate in a given wind velocity. Many researchers have studied Darrieus turbines from different points of view. Hill *et al.* (2009) investigated the self-starting characteristics of an H-rotor Darrieus turbine under steady wind conditions. Tjiu *et al.* (2015) assessed comprehensively the Darrieus vertical axis wind turbine configurations. Recently, Singh *et al.* (2015) studied a three-bladed H-type Darrieus rotor equipped with unsymmetrical S1210 blades for determining its self-starting characteristics. They did their work at various azimuthal positions in different rotor solidities from 0.8 to 1.2.

In order to spread the use of VAWTs, the problems associated with various configurations such as poor self-starting and low initial torque, low power coefficient, poor building integration should be overcome. The main demerits of the fundamental designs included the significant torque fluctuation during each revolution, and the great bending moments on the blades. As aforementioned in the case of Savonius rotors, although they provide high cogging torque, they have low efficiency; on the other hand, Darrieus rotors can provide high efficiency; however, they have low cogging torque. In this study, for improving the self-starting of VAWTs and in order to take advantage of the good features of both the Savonius and Darrieus types, and also to utilize both lift and drag forces, a design of airfoils used in VAWTs is developed. In this design, the airfoils of VAWT are investigated as a J-shaped cross section. This airfoil has been designed by eliminating the one side of airfoil from the maximum thickness toward the trailing edge. The J-Shaped airfoil is a new type of VAWT airfoil using the lift and drag forces simultaneously. Owing to the advantage of drag force, it has a self-start and high cogging torque, thereby improving the efficiency and startup of VAWTs. The airfoils used in this study are NACA0018 and NACA0030 in order to investigate the effect of thickness in J-shaped profiles on the VAWTs

performance.

2. Governing equations

The governing equations for an incompressible flow are the well-known conservation laws, i.e., the continuity equation

$$\frac{\partial u_i}{\partial x_i} = 0 \quad (1)$$

which states that the volume dilatation is equal to zero, and the conservation of momentum in the Multiple Reference Frame (MRF) coordinate

$$\frac{\partial \bar{u}_i}{\partial t} + \bar{u}_j \frac{\partial \bar{u}_i}{\partial x_j} = -\frac{1}{\rho} \frac{\partial \bar{P}}{\partial x_i} + \frac{\partial}{\partial x_j} \left(\nu \frac{\partial \bar{u}_i}{\partial x_j} \right) - \rho \left[2 \cdot \bar{\omega} \times \bar{W} + \bar{\omega} \times \bar{\omega} \times \bar{r} \right] + \frac{\partial \tau_{ij}}{\partial x_j} \quad (2)$$

where \bar{u}_i and \bar{P} , W , ω , ρ and ν are, respectively, averaged velocity, pressure, relative velocity, rotational speed, density and kinematic viscosity. It is noting that the third term of the right hand of Eq. (2) is indicative of rotating the inner domain and is equal to zero in the outer domain. Furthermore, $\bar{\tau}$ is the specific Reynolds Stress tensor described as

$$\tau_{ij} = \overline{u'_i u'_j} \quad (3)$$

3. Turbulence model

For the turbulence closure, according to two-equation Shear Stress Transport (SST) turbulence model proposed by Menter (1994), the combined model of the $\kappa-\omega$ model and the $\kappa-\varepsilon$ model may be written as

$$\begin{aligned} \frac{\partial(\rho\kappa)}{\partial t} + \frac{\partial(\rho u_j \kappa)}{\partial x_j} &= \frac{\partial}{\partial x_j} \left[(\mu + \sigma_\kappa \mu_t) \frac{\partial \kappa}{\partial x_j} \right] - \beta^* \rho \omega \kappa \left[1 + \alpha_1 M_t^2 (1 - F_1) \right] + P_\kappa + \\ &(1 - F_1) \overline{p'' d''} \end{aligned} \quad (4)$$

$$\begin{aligned} \frac{\partial(\rho\omega)}{\partial t} + \frac{\partial(\rho u_j \omega)}{\partial x_j} &= \frac{\partial}{\partial x_j} \left[(\mu + \sigma_\omega \mu_t) \frac{\partial \omega}{\partial x_j} \right] + 2(1 - F_1) \frac{\rho \sigma_{\omega_2}}{\omega} \frac{\partial \kappa}{\partial x_j} \frac{\partial \omega}{\partial x_j} - \\ &\beta \rho \omega^2 + (1 - F_1) \beta^* \alpha_1 M_t^2 \rho \omega^2 - \frac{\rho}{\mu_t} (1 - F_1) \overline{p'' d''} + \alpha \frac{\omega}{\kappa} P_\kappa \end{aligned} \quad (5)$$

with P_κ being the production of turbulence. Turbulent Mach number, $M_t = \sqrt{2k/c^2}$, and pressure dilatation, $\overline{p'' d''} = -\gamma_2 P_\kappa M_t^2 + \gamma_3 \rho \beta^* \kappa \omega M_t^2$, correct the compressibility effects of the turbulent compressible flow. The coefficients of transport equations, σ_κ , σ_ω , α and β are

calculated via the blending function, $F_1 = \tanh \left\{ \min \left[\max \left(\frac{\sqrt{\kappa}}{\beta^* \omega d}, \frac{500g}{\omega d^2} \right), \frac{4\rho\sigma_{\omega_2}\kappa}{CD_{k\omega}d^2} \right] \right\}$, using the following equation

$$\varphi = F_1\varphi_1 + (1 - F_1)\varphi_2 \quad (6)$$

which φ represents each of mentioned coefficients and subscripts 1 and 2 correspond to $\kappa - \omega$ and $\kappa - \varepsilon$ turbulence models, respectively. According to the SST model, the eddy viscosity, μ_t , may be written as

$$\mu_t = \frac{\alpha^* a_1 \kappa}{\max[a_1 \omega, F_2]} \quad (7)$$

which constant a_1 is equal to 0.31 and coefficient F_2 is calculated from the following relation

$$F_2 = \tanh \left\{ \left[\max \left(\frac{2\sqrt{\kappa}}{\beta^* \omega d}, \frac{500g}{\omega d^2} \right) \right]^2 \right\} \quad (8)$$

with $CD_{k\omega} = \max \left[2\rho\sigma_{\omega_2} / \omega (\partial\kappa / \partial x_j) (\partial\omega / \partial x_j), 10^{-10} \right]$ being the positive part of the cross diffusion term and d is the distance to the nearest surface. Because the low-Reynolds effects only modify the near wall boundary layer, low-Re corrections of Wilcox (2006) are applied only to the $\kappa - \omega$ part of the SST model for a^* , a_1 and β^* coefficients.

4. Blade geometry and turbine specifications

To investigate the effect of airfoil thickness used in VAWT on the turbine performance, symmetric airfoils utilizing are NACA0018 and NACA0030. Fig. 1 illustrates a comparison between both airfoil sections. The J-shaped profile of airfoils is produces by means of eliminating the one side of airfoil from the maximum thickness toward the trailing edge, as shown in Fig. 2. Besides, the schematic design of VAWT with and without the J-shaped section is illustrated in Fig. 3. In this study, a fixed pitch $3kW$ straight-bladed Darrieus VAWT is considered, whose characteristics are represented in Table 1.

Table 1 Turbine Characteristics

Characteristics	Values	Abbreviations
Number of Blades	3	B
Far Stream Velocity (m/s)	10	U_∞
Chord (m)	0.27	C
Turbine Height (m)	3.3	H
Turbine Radius (m)	1.85	R
Shaft Radius (m)	0.0575	R_{shaft}

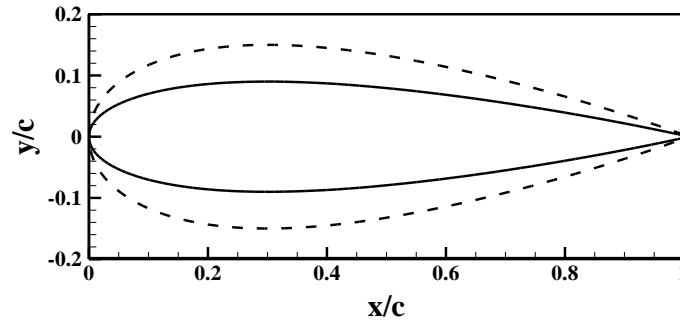


Fig. 1 The comparison of thickness for NACA0018 and NACA0030 airfoils



Fig. 2 The schematic of J-shaped airfoil of NACA0018 and NACA0030

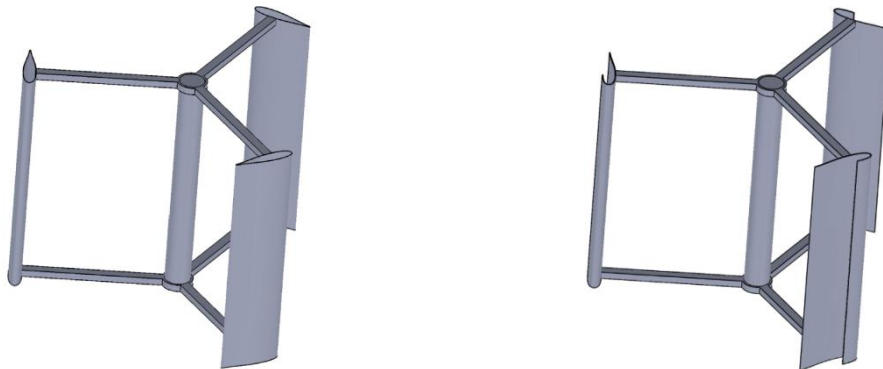


Fig. 3 The schematic design of VAWT with and without J-shaped section

5. The computational domain and meshing

The computational domain is shown in Fig. 4. It is worth noting that the dimensions of computational domain are selected based on the fact that the simulations would represent the unbounded flow around a VAWT. The origin of the coordinate system is placed at the center of the turbine and the x-axis is chosen to be along the main flow direction. As can be clearly seen, the

computational domain comprises two sections including inner rotational domain and outer stationary domain. In the rotational domain, the blades are located on an azimuth angle of 120° relative to each other, as shown in Fig. 5.

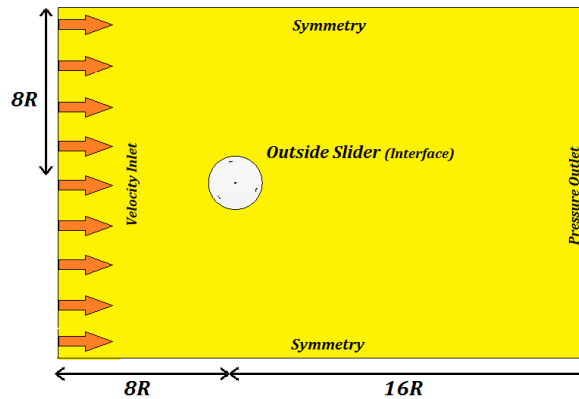


Fig. 4 Details of boundary conditions and computational domain

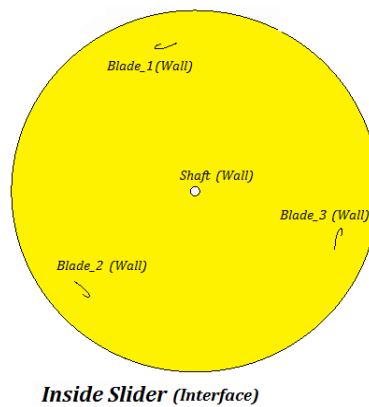


Fig. 5 Situation of locating blades inside interface

In order to generate grids for the computational domains, the construction of the structured and hybrid grid topologies is chosen for the outer stationary domain and inner rotational domain respectively. The final topology of the structured grid can be seen in Fig. 6 and the hybrid grid in relation to the inner rotational domain is illustrated in Fig. 7. Furthermore, the grid system of the turbine blade must have some important features. First, the numerical accuracy of SST models is assured only for specific values of y^+ of the nearest node to the blade surface. It has been reported in the literature that having a maximum value of y^+ between 1 and 5 would give acceptable results (Moshizi *et al.* 2014a,b, Karbasian *et al.* 2015, Srinivasan *et al.* 1995, Streiner *et*

al. 2007). Nevertheless, having a y^+ lower than one leads to more accurate results. In the present study, the maximum value for y^+ is equal to one which gives acceptable results, thereby reducing the computational overhead. The grid generation of physical domain is done by using Pointwise V17.1R2 software. The second criterion is about the orthogonality of grid lines relative to the wall. Better convergence of the solution is achieved when grid lines close to the wall are perpendicular to the wall surface. The boundary layer grid generation is used in the vicinity of the blade surface. In this type of meshing, the grid lines are normal to the surface near the wall, as presented in Fig. 8.

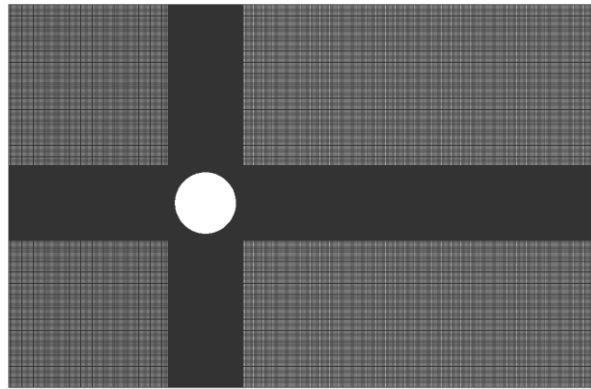


Fig. 6 Structured mesh in the outer stationary domain

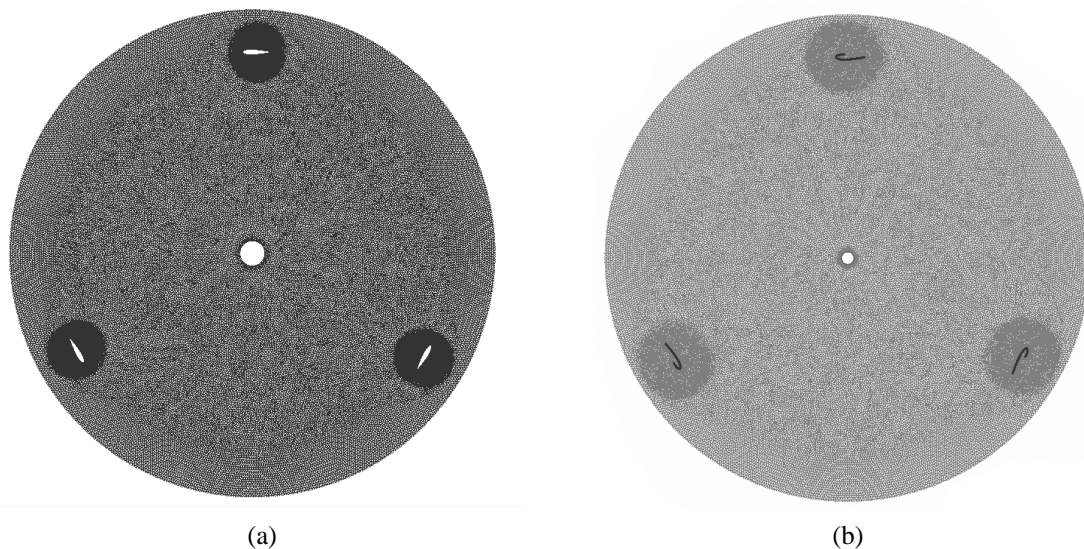


Fig. 7 Hybrid grid in the inner rotational domain, (a) original airfoil and (b) J-shaped profile

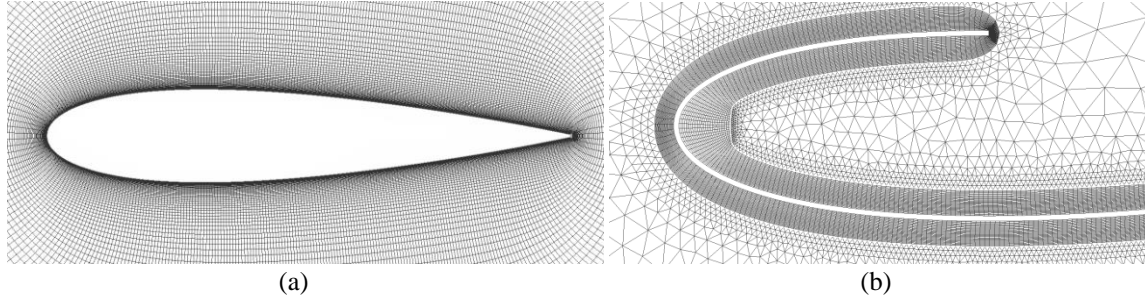


Fig. 8 Boundary layer grid for blade geometry

6. Methodology and boundary conditions

The unsteady flow field around the VAWT is numerically simulated by employing 2D URANS equations. The simulation is carried out by means of OpenFOAM 2.1.1. The system of equations is applied with segregated solver and is discretized based on the finite volume method. Furthermore, the combination of PISO and SIMPLE algorithm called PimpleDyMFoam solver in OpenFoam is used for pressure–velocity coupling. The PimpleDyMFoam solver is a transient solver developed for turbulent incompressible flows. This solver is a modification of the pimpleFoam solver supporting meshes of dynamicFvMesh class. The class is a base class for meshes that can move and/or change topology.

PISO is an acronym for Pressure Implicit Splitting of Operators for time dependent flows while SIMPLE stands for Semi-Implicit Method for Pressure Linked Equations which is used for steady state problems. In the SIMPLE algorithm, a pressure correction term is used while the velocity corrections are neglected because they are unknown. This results in a rather slow convergence. The PISO algorithm also neglects the velocity correction in the first step, but then performs one in a later stage, leading to additional corrections for the pressure (The open source cfdtoolkids, 2010).

The turbulence effect on flow field is accounted for using the $\kappa-\omega$ SST turbulence model. At the point of boundary conditions, for the entrance and discharge of fluid in computational domain, the velocity inlet and pressure outlet conditions are selected respectively. For two far-field boundaries, a zero-flux condition is used for all variables, since the boundaries are adequately far from the turbine. Moreover, no-slip condition for blade surfaces is selected to set up the wall condition. For a sliding interface type of boundary, the code performs mesh manipulation after each time step. In this study, the General Grid Interface (GGI) method is used for the sliding interface. In this model, a set of equations controlling the flow variables between the GGI rotational domain and the GGI stationary domain is derived from basic FVM discretisation reasoning. The equations present that consistent and conservative discretisation across the interface is achieved using weighted interpolation of the following form (Beaudoin and Jasak 2008, Ghasemi *et al.* 2014)

$$\phi_{S_i} = \sum_n W_{R_n - to - S_i} \times \phi_{R_n} \quad (9)$$

$$\phi_{R_j} = \sum_n W_{S_m - to - R_j} \times \phi_{S_m} \quad (10)$$

The values of ϕ_{S_i} and ϕ_{R_i} are flow variables in the stationary and rotational domains respectively. In order to remain conservative the interface discretisation, the following constraints are presented as

$$\sum_m W_{S_m-to-R_i} = 1.0 \quad (11)$$

$$\sum_n W_{R_n-to-S_j} = 1.0 \quad (12)$$

$$W_{S_m-to-R_j} \times |S_{M_n}| = W_{R_n-to-S_i} \times |S_{R_m}| = |S_{\cap R-to-S}| \quad (13)$$

where $W_{S_m-to-R_j}$, $W_{R_n-to-S_i}$, $|S_{M_n}|$ and $|S_{R_m}|$ are, respectively, indicative of the stationary facet to rotational facets weighting factor, rotational facet to stationary facets weighting factor, surface area of stationary facet, and surface area of rotational facet.

It is interesting to note that since the simulations are a 2D cross section of the turbine, the struts (arms) are not included. Therefore, the power loss caused by them is not included. In addition, the losses resulted in by the 3D effects are not considered. As a result, the power coefficient produced is expected to have a value higher than those obtained experimentally (Almohammadi *et al.* 2011).

7. Grid independency and validation

To validate, the numerical results obtained are assessed in comparison with experimental and numerical results of Bravo *et al.* (2007) and Lanzafame *et al.* (2014) respectively. Accordingly, the studied VAWT for validation of methodology of problem is a 3-blade rotor with NACA0015 airfoil recommended by Bravo. Moreover, the turbulence model used by Lanzafame is $\kappa-\omega$ SST. To investigate the grid independency for the accuracy of the numerical solution, four different meshes of M1, M2, M3, and M4 are studied. The specifications of each grid are shown in Table 2 and the power coefficient at $\lambda=1.6$ is determined for these grids. Moreover, Fig. 9 shows the variation of rotor power across azimuth angle in the four different grids. As is evident, there is a little difference between the numerical results of M3 and M4 meshes. As a result, further results are obtained using the mesh of M3 mesh.

Table 2 Calculating the power coefficient from four different grids to study grid independence

Grid	Number of Cell on Airfoil (up \times down)	Total of cells	First cell height	Aspect Ratio into boundary layer	Power Coefficient ($\lambda=1.6$)
M1	50 \times 50	121465	0.000137	1.03	0.1638
M2	100 \times 100	196853	0.000137	1.03	0.3741
M3	200 \times 200	454325	0.000137	1.03	0.3437
M4	400 \times 400	1345513	0.000137	1.03	0.3445

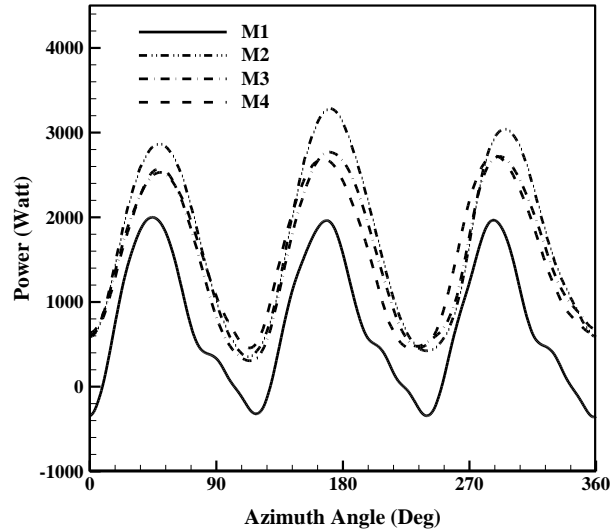


Fig. 9 The study of grid dependency via power across azimuth angle at $\lambda = 1.6$

As can be clearly seen in Fig. 10, the power coefficient results are in good agreement with the experimental data than numerical results by Lanzafame. Although, at the optimum λ , the present results may have a considerable difference with experimental results, it well predicts the power coefficient trend at the other wide range of λ .

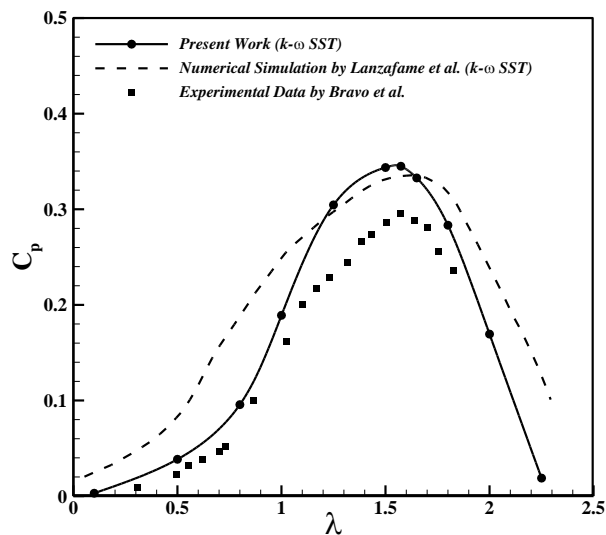
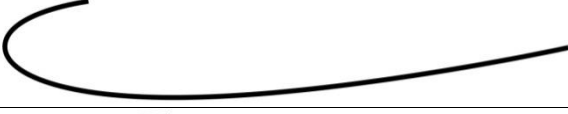




Fig. 10 The obtained power coefficient compared with the experimental data and numerical simulation

Table 3 Geometry of the different J-shaped Profiles

Cutting Position (*)	Cross Section of NACA0018 Airfoil
0.5-J	
J	
1.5-J	

(J: The distance between maximum thickness and leading edge) (*)

8. Results and discussion

The paper investigates the performance of VAWT with the J-shaped blades. Since J-shaped blades utilize the lift and drag forces simultaneously, the turbine performance at low tip speed ratios (TSRs) enhances. Therefore, it is expected that using these blades improves the starting torque and output power. Firstly, in order to find an optimum J-shaped profile acquiring the best performance of wind turbine, a 3kW J-Shaped Darrieus type VAWT is investigated numerically. The J-shaped profile is designed by means of eliminating a portion of pressure side of the NACA0018 airfoil. Specifications of the J-shaped profiles are presented in Table 3. Fig. 11 shows the variation of torque with respect to azimuth angle during one revolution of the turbine at TSR=1.00 for the J-shaped profiles. The results indicate that the performance of turbine is optimized for the J-shaped profile. Moreover, by employing this J-shaped profile, the torque amplitude is decreased. Finally, the vibrations and fatigue stress acting on the rotor and shaft reduce.

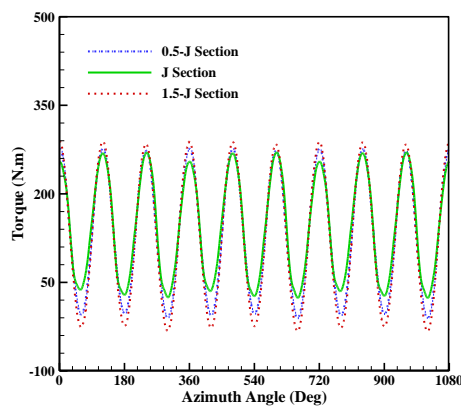


Fig. 11 Effect of cutting position of J-shaped profile on the torque variation for the three cycles at $\lambda = 1.0$

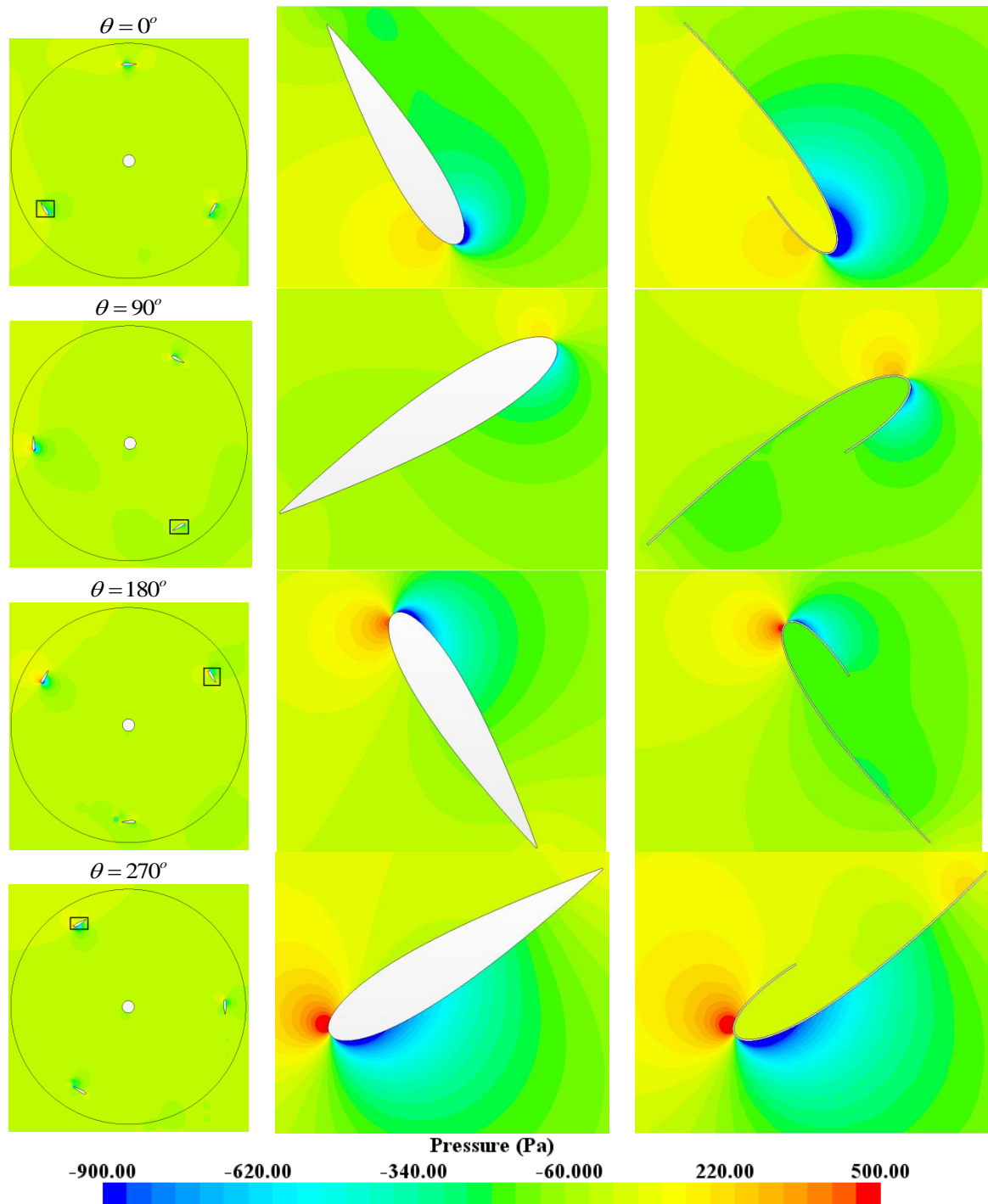


Fig. 12 Effects of J-shaped profile (NACA0018) on pressure distributions for one complete rotation of the VAWT

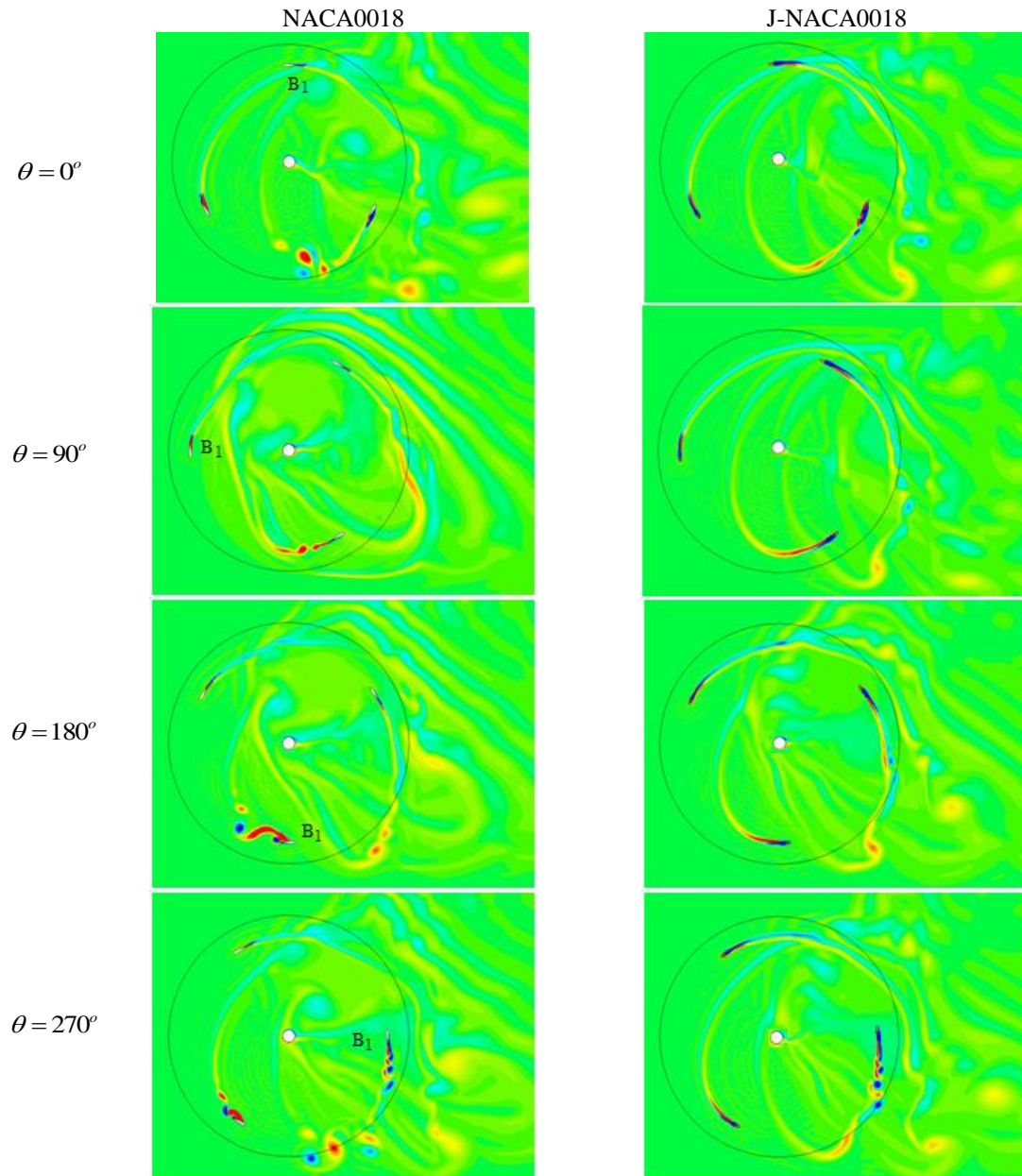


Fig. 13 Effects of J-shaped profile on vorticity distributions for one complete rotation of the VAWT

Fig. 12 shows the pressure distributions for one complete rotation at four different azimuth angles with the NACA0018 and J-NACA0018 (J-shaped profile of NACA0018). As is evident, the pressure gradient between both sides in J-shaped profile is more than the airfoil profile. As a result, the blades with a J-shaped profile can generate higher torque. Needless to say, the maximum and

minimum pressure gradients between both sides belong to the J-shaped profiles in 270° and 90° azimuth angle respectively, due to the high rate of being exposed to the wind direction. Fig. 13 illustrates vorticity counters at different azimuth angles covering a complete rotation with NACA0018 and J-NACA0018 profiles. In this figure, the different modes of B1 blade which is mentioned in Fig. 12 have been described at four azimuth angles. In $\theta = 0^\circ$, the maximum lift force is exerted on both profiles; in contrast, in $\theta = 180^\circ$, these profiles produce the maximum drag force in which the generated drag force from J-NACA0018 is more than NACA0018 because J-NACA0018 utilizes a cup-shaped profile in its own leading edge (similar to Savonius turbine performance). Moreover, in regard to B1 blade in $\theta = 90^\circ$, the vortices form and in $\theta = 270^\circ$, these vortices increase and reach its own peak after which it decreases gradually until $\theta = 0^\circ$. As can be clearly seen, the J-NACA0018 blade experiences the smaller vortices and leads vortices to dissipate faster. In conclusion, it can be observed that the turbulence, noise, and fatigue stress on the turbine shaft and the bearing of VAWT with J-NACA0018 blade decrease because the wake narrows down its region in the downwind of the turbine.

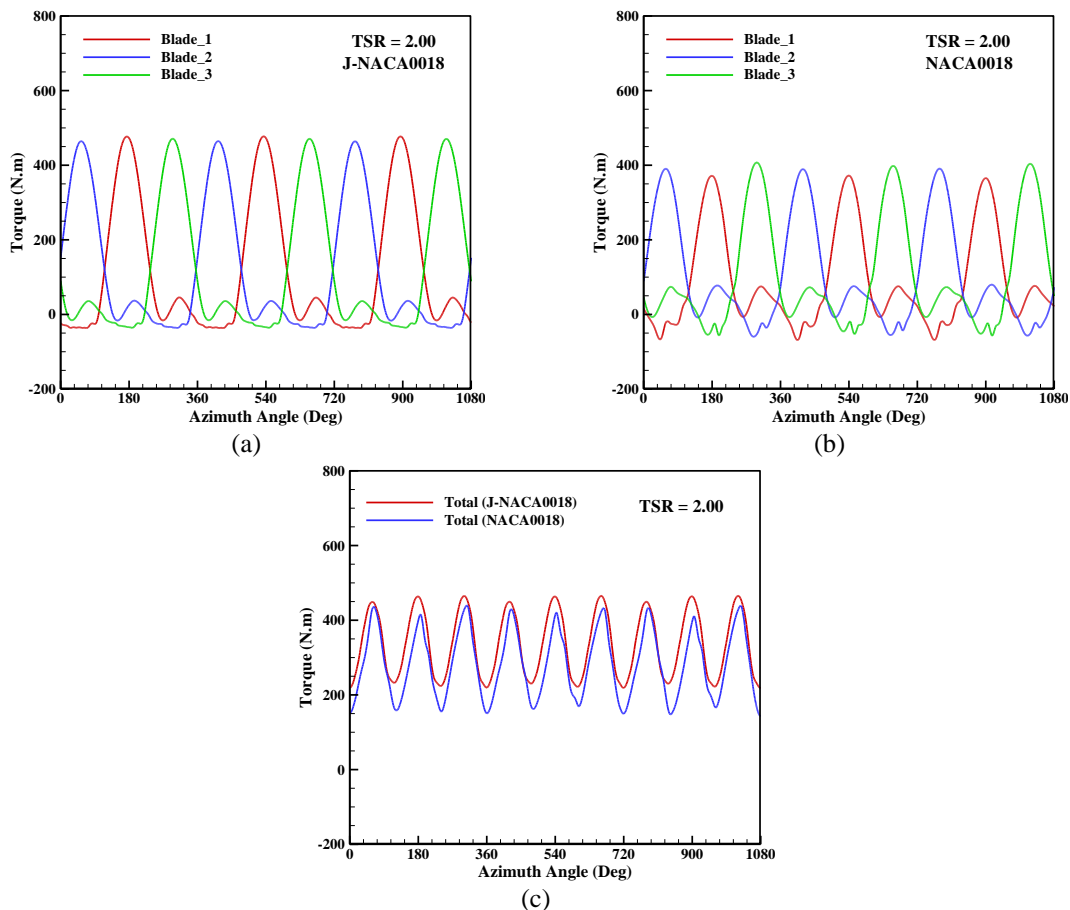


Fig. 14 Effects of J-shaped profile on the torque ripple (a and b) and total torque (c) for the three cycles at $\lambda = 2.0$

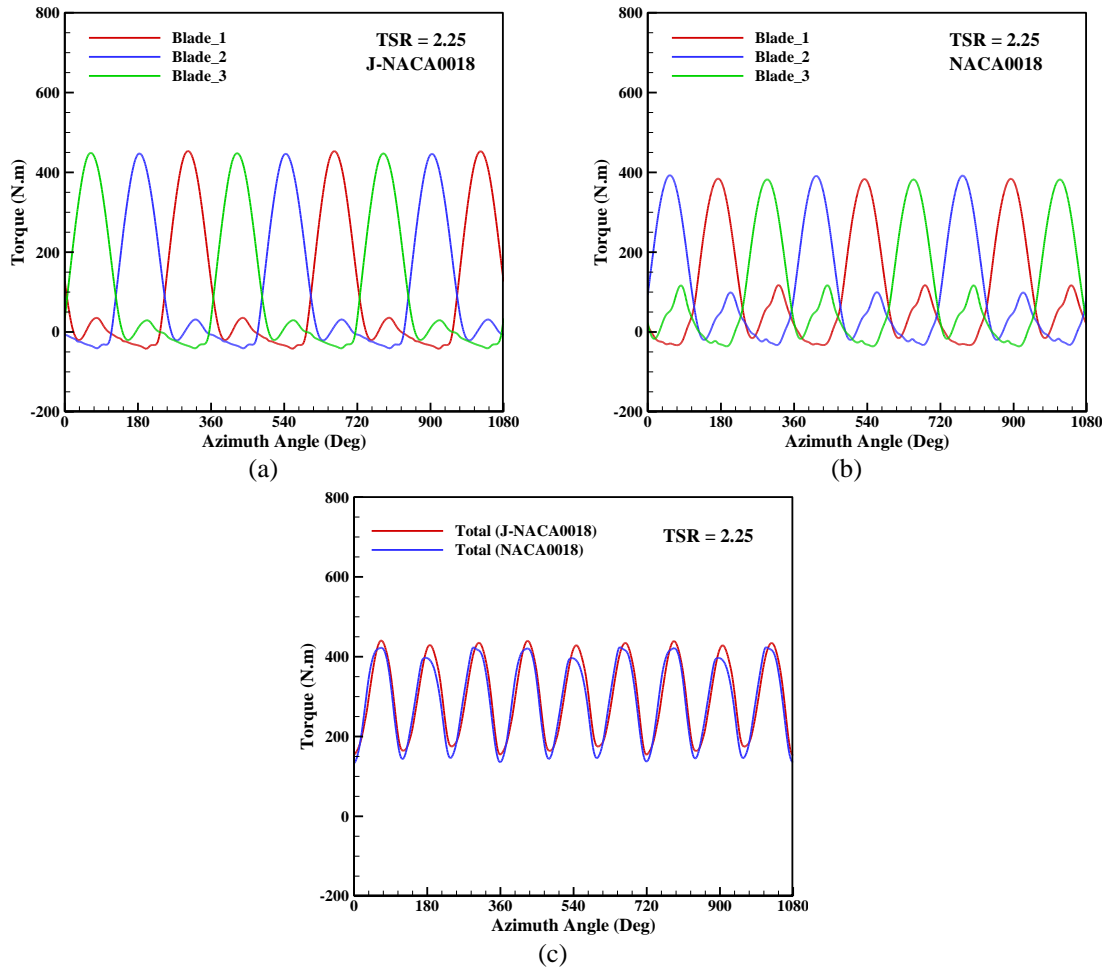


Fig. 15 Effects of J-shaped profile on the torque ripple (a and b) and total torque (c) for the three cycles at $\lambda = 2.25$

Figs. 14 and 15 illustrate the effects of J-shaped profile in NACA0018 airfoil on torque variations for three cycles at optimum TSRs in which $\lambda = 2.0$ and $\lambda = 2.25$ relates to J-NACA0018 and NACA0018 respectively. As is evident, the blades with J-shaped profiles produce the greater torque (Figs. 14(a) and 14(b), 15(a) and 15(b)); hence, the average of the overall torque per cycle is higher (Figs. 14(c) and 15(c)). In addition, the effects of J-shaped profile in NACA0030 airfoil on torque variations for three cycles at its own optimum TSRs are shown in Figs. 16 and 17. The similar results related to the effects of J-shaped profile are derived from these figures. It can be asserted that improving the generated torque resulting from J-shaped NACA0030 can be corresponded to the higher thickness of the airfoil because of increasing the drag force.

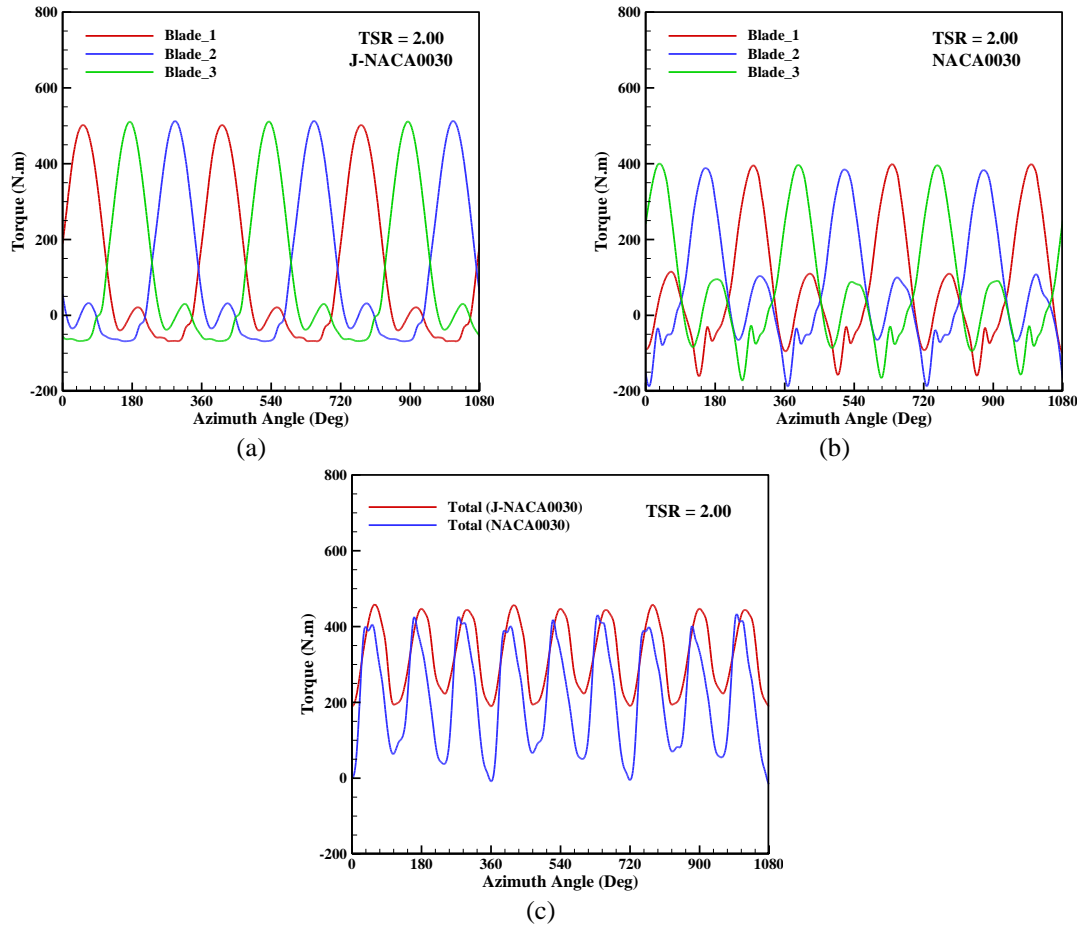


Fig. 16 Effects of J-shaped profile on the torque ripple (a and b) and total torque (c) for the three cycles at $\lambda = 2.0$

Fig. 18 reveals the impacts of airfoils thickness and their J-shaped profile on the power coefficient, C_p , in two studied NACA airfoils. It is obvious that the NACA0018 performance is better than its counterpart's performance due to its aerodynamic characteristics, as presented in Fig. 18(a). The better performance of J-shaped profiles with respect to cogging torque and optimum power coefficient in comparison with their references is illustrated in Figs. 18(b) and 18(c). The effect of J-NACA0030 airfoil on turbine performance at low TSRs is further because of its higher thickness, as can be obviously seen in Fig. 18(d).

The other influential parameter in turbine design is the torque coefficient; hence, the effects of thickness and J-shaped profile on this parameter are investigated in Fig. 19. In the reference airfoils, the torque coefficient has a higher amount in NACA0018, while in J-shaped airfoils, J-NACA0030 has higher torque coefficients at low TSRs, as shown in Fig. 19(a) and 19(b). As is evident, making J-shaped airfoils leads torque coefficients to modify at initial TSRs until its optimum (Figs. 19(c) and 19(d)).

Table 4 reveals the percentage of increasing cogging torque due to using J-shaped profiles in

VAWTs. As can be vividly realized, this increase in cogging torque of VAWT with NACA0030 is further because the higher thickness plays an important role in the improvement of cogging torque of J-shaped profiles.

Table 5 presents the beneficial data regarding the average output power and power coefficient at different TSRs for the rated wind speed. The bold data corresponds to optimum TSRs of J-shaped profiles and NACA airfoils whose quantities are 2 and 2.25 sequentially. By substituting J-NACA0018 section for its own reference airfoil in the turbine blade, the turbine output power at optimum TSRs of J-shaped and NACA sections increases by 20% and 3.5%, while by exploiting NACA0030 instead of NACA0018 section, the turbine output power intensifies by 34% and 12.6% respectively. In order to elucidate the aforementioned data in Table 3, the maximum power point tracking (MPPT) for four different status of the blade section including NACA airfoils and J-shaped profiles are indicated in Fig. 20. According to this figure and Fig. 21, it can be concluded that, in a fixed rotational speed, making J-shaped profile from an airfoil with a higher thickness leads to a higher increase in the output power.

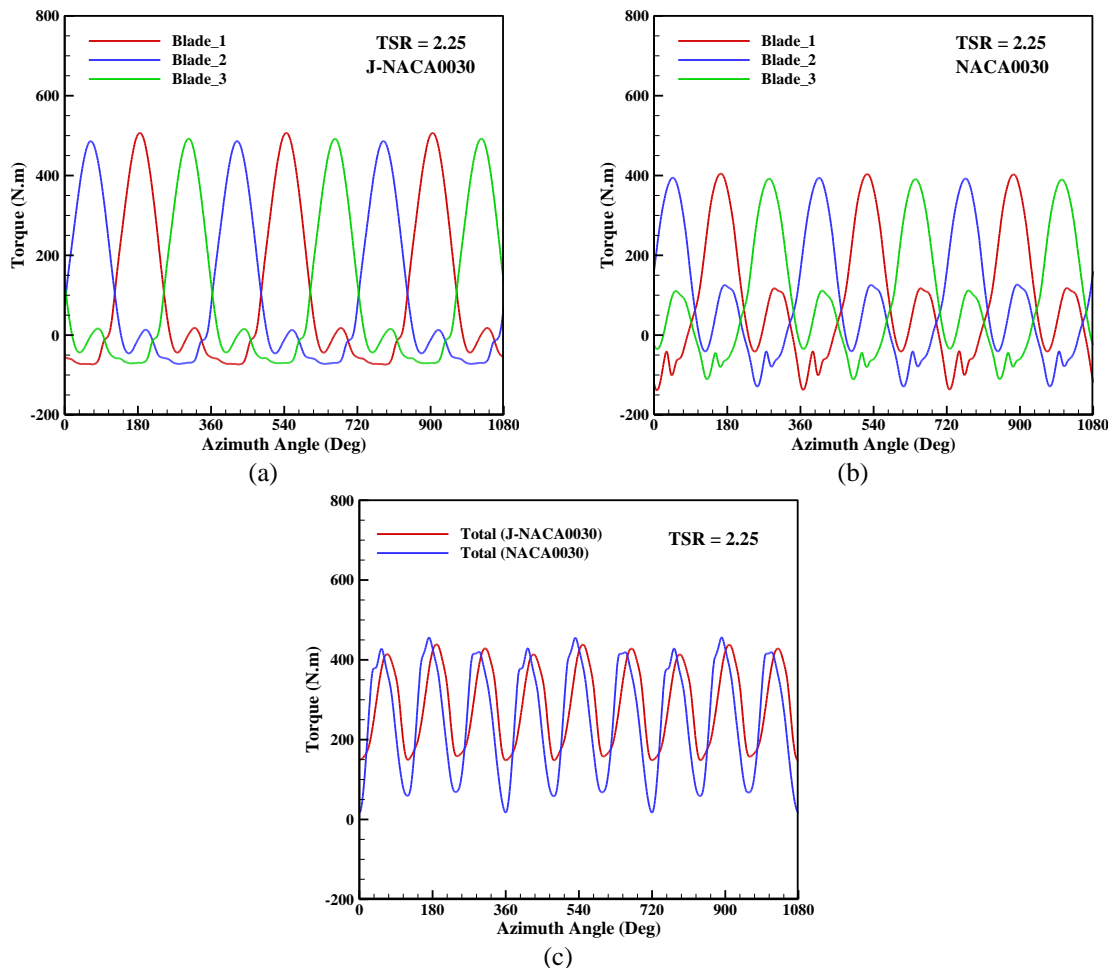


Fig. 17 Effects of J-shaped profile on the torque ripple (a and b) and total torque (c) for the three cycles at $\lambda = 2.25$

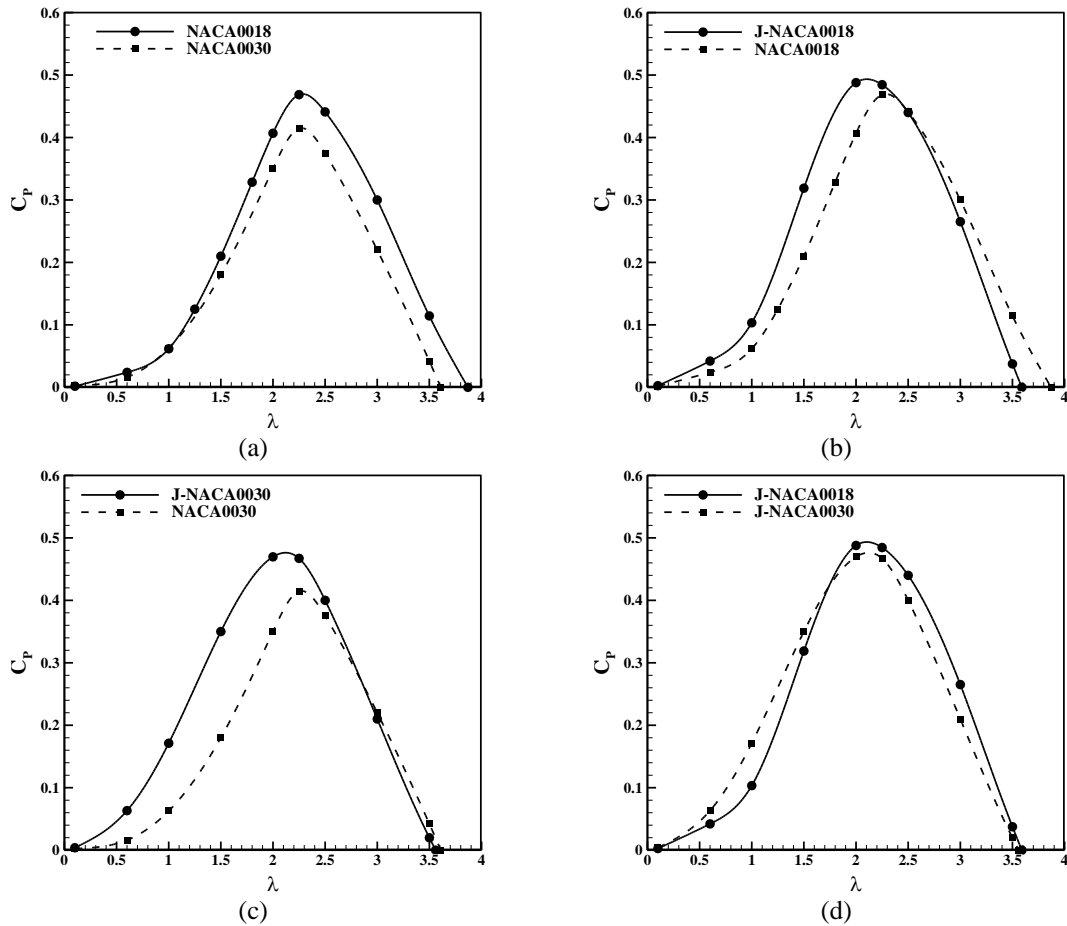


Fig. 18 Effects of airfoil thickness and J-shaped profile on the turbine performance in terms of the power coefficient

Table 4 The percentage of Cogging torque improvement on the J-shaped profiles

Section	Cogging Torque (N.m)	Improvement
NACA0018	2.204	46.8%
J- NACA0018	3.237	
NACA0030	2.933	64.7%
J- NACA0030	4.832	

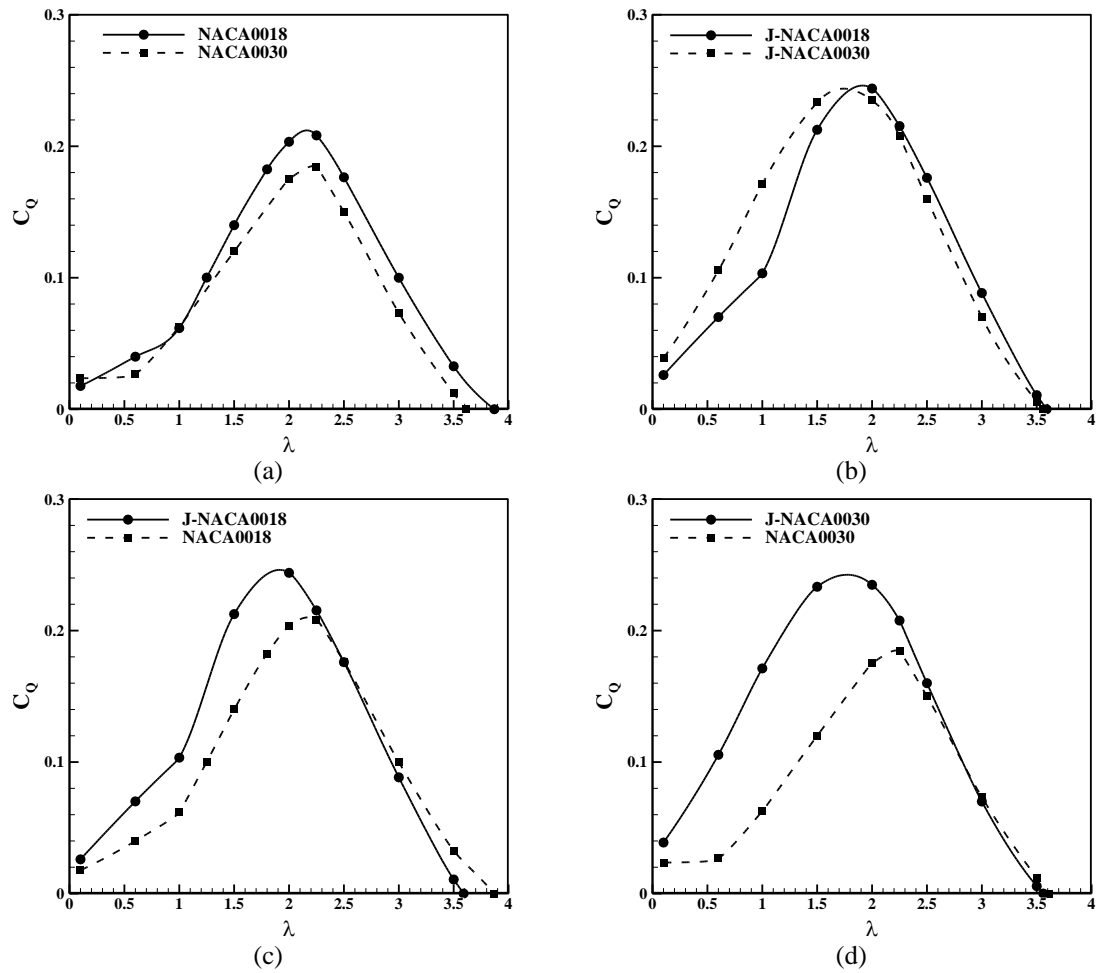


Fig. 19 Effects of airfoil thickness and J-shaped profile on the torque coefficient

Table 5 Average output power and power coefficient at different TSRs for rated wind speed

λ	ω	Power (Watt)			
		NACA0018	J-NACA0018	NACA0030	J-NACA0030
0.10	5.16	13.24	19.44	17.62	29.02
0.60	30.97	179.32	314.57	120.06	473.49
1.00	51.62	461.52	772.90	469.36	1280.58
1.50	77.43	1570.51	2384.49	1346.15	2617.52
2.00	103.24	3042.38	3648.49	2617.52	3512.33
2.25	116.14	3504.38	3623.64	3101.39	3493.80
2.50	129.04	3298.07	3290.60	2804.48	2991.45
3.00	154.85	2243.59	1982.88	1645.30	1570.51
3.50	180.66	855.05	280.45	314.10	147.97

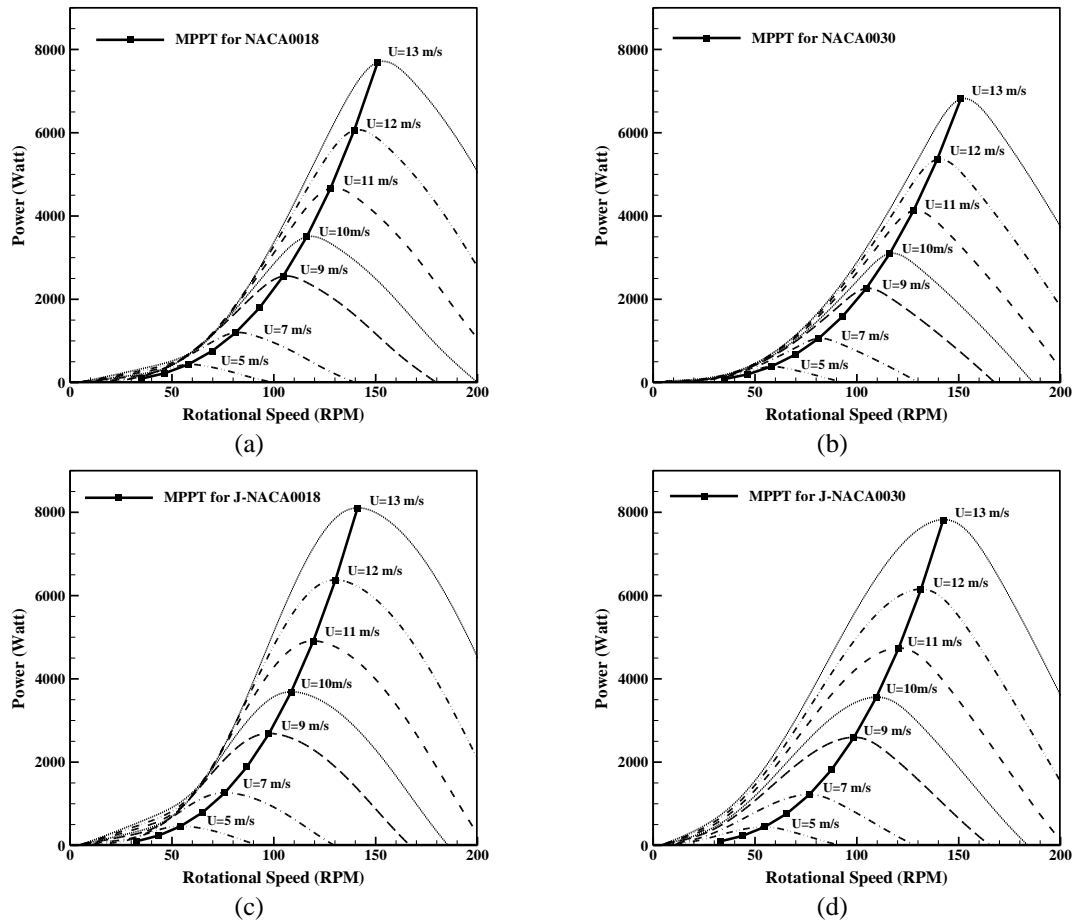


Fig. 20 Effects of airfoil thickness and J-shaped profile on the maximum power point tracking (MPPT) curve

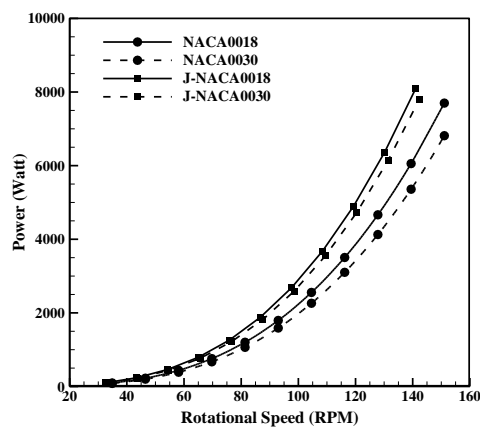


Fig. 21 Comparison among the maximum power point tracking (MPPT) curves

9. Conclusions

Nowadays, there are widespread vertical axis wind turbines (VAWTs) consisting of two major types, the Darrieus rotor and Savonius rotor. Darrieus wind turbines rotate around a central axis due to the lift produced by the rotating airfoils, whereas a Savonius rotor rotates due to the drag created by its blades. A Darrieus rotor can provide high efficiency; however, it has low cogging torque; on the other hand, although a Savonius rotor provides high cogging torque, it has low efficiency. This paper presents the new approach which can improve the performance and cogging torque of VAWTs. In this method, the blades section comprises J-shaped profiles obtained through eliminating the pressure side of airfoil from the maximum thickness toward the trailing edge. Consequently, this type of VAWT exploits the lift and drag forces simultaneously in order to modify its startup and performance. The main purpose in the current study is to investigate the effects of blade thickness on its aerodynamic characteristics of wind turbine with J-shaped profiles. For this purpose, a two-dimensional computational analysis was conducted to simulate the fluid flow of the VAWTs with two airfoils named NACA0018 and NACA0030. The Reynolds Averaged Navier-Stokes (RANS) equations were closed using the two-equation Shear Stress Transport (SST) turbulence model. The flow field was solved by OpenFOAM 2.1.1 software. The results obtained indicate that using thicker J-shaped profiles in the blades section leads to higher performance and cogging torque. Using NACA0030 instead of NACA0018 in order to make J-shaped profiles in the structure of VAWT blades causes the cogging torque and power to increase by 64.7% and 34% respectively which is more than NACA0018 quantities about 18% and 14%.

References

- The open source cfdtoolkids (2010), "User guide", <http://www.openfoam.com> [Online].
- Akwa, J.V., Vielmo, H.A. and Petry, A.P. (2012), "A review on the performance of Savonius wind turbines", *Renew. Sust. Energ. Rev.*, **16**, 3054-3064.
- Almohammadi, K.M., Ingham, D., MA, L. and Pourkashanian, M. (2011), "CFD modelling investigation of a straight-blade vertical axis wind turbine", *Proceedings of the 13th International Conference on Wind Engineering*, Amsterdam, Netherland.
- Beaudoin, M. and Jasak, H. (2008), "Development of a generalized grid interface for turbomachinery simulations with OpenFOAM", *Proceedings of the Open Source CFD International Conference*, Berlin, Germany, December.
- Bos, R. (2012), *Self-starting of a small urban Darrieus rotor*, Master of Science, Delft University of Technology, Netherland.
- Bravo, R., Tullis, S. and Ziada, S. (2007), "Performance testing of a small vertical-axis wind turbine", *Proceedings of the 21st Canadian Congress of Applied Mechanics (CANCAM07)*, Toronto, Canada, June.
- Darrieus, G. (1931), "Turbines having its rotating shaft transverse to the flow of the current", US patent no. 1835 018 patent application.
- Fernando, M.S.U.K. and Modi, V.J. (1989), "A numerical analysis of the unsteady flow past a Savonius wind turbine", *J. Wind Eng. Ind. Aerod.*, **32**, 303-327.
- Fujisawa, N. (1992), "On the torque mechanism of Savonius rotors", *J. Wind Eng. Ind. Aerod.*, **40**(3), 277-292.
- Ghasemi, A., Pathak, A. and Raessi, M. (2014), "Computational simulation of the interactions between moving rigid bodies and incompressible two-fluid flows", *Comput. Fluids*, **94**, 1-13,.
- Ghasemi, A., Olinger, D. and Tryggvason, G. (2015), "Numerical simulation of tethered underwater kites for power generation", *Proceedings of the ASME 2015 International Mechanical Engineering Congress &*

- Exposition, IMECE 2015*, Houston, USA, November.
- Hill, N., Dominy, R., Ingram, G. and Dominy, J. (2009), "Darrieus turbines: The physics of self-starting", *Proceedings of the Institution of Mechanical Engineers, Part A: Journal of Power and Energy*, **223**, 21-29.
- Kamoji, M.A., Kedare, S.B. and Prabhu, S.V. (2009), "Performance tests on helical Savonius rotors", *Renew. Energ.*, **34**(3), 521-529.
- Karbasian, H.R., Moshizi S.A. and Maghrebi M.J. (2015), "Dynamic stall analysis of S809 pitching airfoil in unsteady free stream velocity", *J. Mechanics*, FirstView.
- Khare, V., Nema, S. and Baredar, P. (2016), "Solar-wind hybrid renewable energy system: A review", *Renew. Sust. Energ. Rev.*, **58**, 23-33.
- Lanzafame, R., Mauro, S. and Messina, M. (2014), "2D CFD modeling of H-darrieus wind turbines using a transition turbulence model", *Energy Procedia*, **45**, 131-140.
- Menet, J.L. (2004), "A double-step Savonius rotor for local production of electricity: a design study", *Renew.Energ.*, **29**(11), 1843-1862.
- Menter, F.R. (1994), "Two-equation eddy-viscosity turbulence models for engineering applications", *AIAA J.*, **32**(8), 1598-1605.
- Modi, V.J. and Fernando, M.S.U.K. (1989), "On the performance of the savonius wind turbine", *J. Solar Energy Eng.*, **111**(1), 71-81.
- Moshizi, S.A., Madadi, A. and Kermani, M.J. (2014a), "Comparison of inviscid and viscous transonic flow field in VKI gas turbine blade cascade", *Alexandria Eng. J.*, **53**(2), 275-280.
- Moshizi, S.A., Nakhaei, M.H., Kermani, M.J. and Madadi A. (2014b), "Development of a numerical based correlation for performance losses due to surface roughness in axial turbines", *J. Mechanics*, **30**(6), 631-642.
- Saha, U.K., Thotla, S. and Maity, D. (2008), "Optimum design configuration of Savonius rotor through wind tunnel experiments", *J. Wind Eng. Ind. Aerod.*, **96**(8-9), 1359-1375.
- Savonius, S. J. (1931), "The S-rotor and its applications", *Mech. Eng.*, **53**, 333-338.
- Siddiqui, M.S., Durrani, N. and Akhtar, I. (2015), "Quantification of the effects of geometric approximations on the performance of a vertical axis wind turbine", *Renew. Energ.*, **74**, 661-670.
- Singa, M.A., Biswas, A. and Misra, R.D. (2015), "Investigation of self-starting and high rotor solidity on the performance of a three S1210 blade H-type Darrieus rotor", *Renew. Energ.*, **76**, 381-387.
- Srinivasan, G.R., Ekaterinaris, J.A. and McCroskey, W.J. (1995), "Evaluation of turbulence models for unsteady flows of an oscillating airfoil", *Comput. Fluids*, **24**(7), 833-861.
- Streiner, S., Kramer, E., Eulitz, A. and Armbruster, P. (2007), "Aeroelastic analysis of wind turbines applying 3D CFD computational results", *J. Physics: Conference Series*, **75**.
- Tjiu, W., Marnoto, T., Mat, S., Ruslan, M.H. and Sopian, K. (2015), "Darrieus vertical axis wind turbine for power generation I: Assessment of Darrieus VAWT configurations", *Renew. Energ.*, **75**, 50-67.
- Tong, W. (2010), *Wind Power Generation and Wind Turbine Design*, WIT press, Kollmorgen Corporation, USA.
- Wilcox, D.C. (2006), *Turbulence Modeling for CFD*, DCW industries.